MODAL DESIGN OPTIMIZATION FOR PANEL FLUTTER AND BUCKLING

Kevin A. McHugh*[1], Cate Leszcz[2], and Joshua Deaton[1]

[1]U.S. Air Force Research Laboratory, Wright-Patterson Air Force Base, OH, USA,
kevin.mchugh.3@us.af.mil, joshua.deaton@us.af.mil
[2]University of Colorado, Boulder, CO, USA, cate.leszcz@colorado.edu

Keywords: Aerothermoelasticity, optimization, flutter, buckling

Abstract: This work investigates a new method to design aircraft skin panels to minimize weight while providing sufficient strength to withstand both buckling due to aerodynamic heating and flutter due to dynamic pressure over the panel. In this work, mass minimization is done via an optimization of panel thickness distribution as opposed to fill-void techniques or methods of adding discrete stiffeners found in the literature or in practice. The thickness distribution and therefore optimization problem is further reduced in numerical order by utilizing a Galerkin projection of global thickness basis functions. The developed tool results in a 6-17% reduction in weight for an optimized panel for thermal buckling stability when compared to the optimally thin flat panel.

1 INTRODUCTION

Panel flutter is a long-studied phenomenon critical to aircraft design in which the thin exterior panels of the aircraft—having been subjected to aerodynamic pressure and heating—tend to lose elastic stability and either statically buckle or dynamically flutter. Early work on the physics and the modeling of the problem is summarized in a survey by Dowell [1], and a more recent survey is collected by Mei [2]. Recently there has been a resurgence of research interest in panel flutter in high-speed flow, with a noted increase in experimental work [3–5] to validate, inform, and otherwise cooperate with advances in computational modeling techniques [6]. A substantial review of these techniques is given by McNamara and Friedman [7].

Critical to the phenomena of panel flutter is the design of the panels themselves. The nature of design is to minimize weight while providing sufficient strength to withstand both buckling due to heating and flutter due to flow over the panel. Recently, using piston theory aerodynamics and linear finite elements, Stanford and Beran [8] implemented a SIMP-based design optimization technique to position material within a uniform thickness panel to minimize weight with respect to both flutter and buckling constraints. Deaton and Grandhi [9] later demonstrated that geometric nonlinearities are significant for problems with thermal loads. Lee and Bhatia [10] analyzed the impact of corrugations in the panels versus flat panels, and found that the corrugations increase the thermoelastic buckling stability. Bhatia and Beran [11] utilized a finite element formulation to model an Euler-Bernoulli beam subjected to Euler-based flow, and determined the optimized thickness distribution of the beam to be similar in shape to the fundamental flutter shape with a 22% weight reduction compared to the optimal flat beam.

From these studies, it is hypothesized that there is a practical benefit to the thickness distribution approach of Bhatia and Beran, since it may prove more easily manufacturable than a void fill or density gradient technique and simpler to test experimentally at small scales than corrugated plates. To improve the technique, we propose the use of a reduced order modal structural model coupled to a low order piston theory-based fluid solver to reduce the dimensionality of the optimization problem. Results by this author [12] have been published for the Euler-Bernoulli beam version of this problem and demonstrated a 40% weight savings for this simplified two-dimensional problem, while reducing the dimensionality of the problem from the higher order techniques employed previously [11]. However, stress concentrations of the streamwise edges of the panels are not captured by the beam model, and the previous model evaluated only up to the stability boundary, but could not capture a response beyond the post-critical heating or flow physics.

The objective of this work is therefore to demonstrate a weight-optimized three-dimensional panel for thermal buckling and high-speed flutter stability. For this purpose, a computationally efficient model is developed from the Galerkin modal expansion of the Von Karman plate equations, including a nonlinear stretching term as a geometric nonlinearity so that post-critical behavior such as post-buckled states and post-flutter limit cycle oscillations (LCO) may be observed. The aerodynamic forces are modeled with first order piston theory, and the thermal model is a simple temperature gradient between the plate and its boundary conditions, which in turn affects the model stiffness. A similar model has been shown to correlate well with experiment [6, 13]. Weight minimization is performed by optimizing the thickness distribution of the plate in the streamwise and spanwise directions by employing a Galerkin-based modal thickness distribution to reduce the dimensionality of the optimization problem.

A secondary objective of this paper is to explore the design of a baseline constant-thickness panel using higher fidelity methods to provide additional insight on the behavior of the panel under aerothermodynamic loads. This is accomplished using Abaqus finite element analyis (FEA) software with in-house Eckert's reference enthalpy codes to determine mechanical stresses based on aerothermal loads. The second author performed this work to satisfy partial requirement of the Ohio State University's bachelors degree with honors research distinction [14].

It should be noted that this work is the first phase of a larger design project, with the overarching objective of demonstrating multi-fidelity design optimization practices by considering a range of fidelities: from low-fidelity modal structures with piston theoretic aerodynamics, to finite-element structures coupled with aerodynamics and thermodynamics, to experimental wind tunnels. Riley's recent experimental study [4] demonstrated the measurement of the aerothermoelastic response of a thin panel in the AFRL Mach 6 High Reynolds Number Facility (M6HRF), which is the intended test facility for this study. The aerodynamic properties used herein match those found in this facility, to compare with a future experimental campaign to validate this computational work.

The multi-fidelity nature of the research will consider best practices and aim to answer questions such as "Does using lower-fidelity models for many design iterations yield realizable design spaces for the higher-fidelity models?" and "Should higher-fidelity modeling be used in parallel with the lower-fidelity modeling?"

Therefore, the main objectives of this ongoing work are the following:

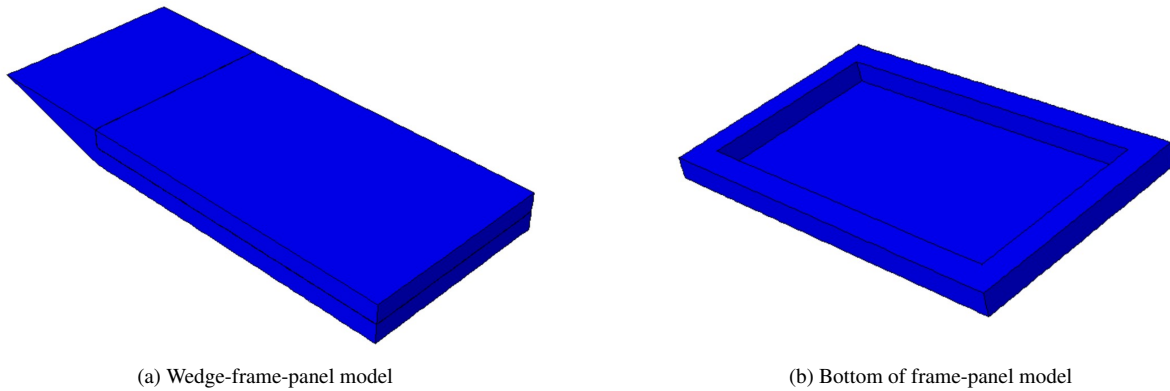1. Demonstrate the utility of low-fidelity modal modeling techniques for optimization prac-

(a) Wedge-frame-panel model   (b) Bottom of frame-panel model

Figure 1: CAD models of wedge and panel

tices

2. Design a panel which is mass-optimized for:
   (a) aerodynamic loading only; constrained so no flutter occurs
   (b) thermal loading only; constrained so no buckling occurs
   (c) aerothermal loading; constrained so neither buckling nor flutter occur
   (d) aerothermal loading; a statically stable buckled panel with no flutter
3. Analyze design with high-fidelity nonlinear finite element method to correlate with low-fidelity modal method
4. For future experimental campaign, choose plate design for:
   (a) A flat plate constrained to be statically stable with a factor of safety requirement set by the tunnel rules
   (b) A variable thickness plate constrained so neither buckling nor flutter occur
   (c) A flat plate constrained to statically buckle but remain flutter-free
   (d) A variable thickness plate constrained to statically buckle but remain flutter-free

In this paper, objectives 1, 2b-c, 3, and 4a-b are met. Paths forward for remaining objectives are given in the conclusions.

2 MODEL SETUP

2.1 Simplified Wind Tunnel Setup

The general wedge-frame-panel setup resembles Riley's experimental setup [15]. The entire assembly is made of Stainless Steel 17-4PH H900, and is shown in Fig. 1a. It is important to note that the panel and wedge are separate parts, and that there is a cavity beneath the panel that is not visible in Fig. 1a. An image with the wedge omitted of the frame-panel model rotated to show the underside of the panel is shown in Fig. 1b to illustrate the cavity. The panel, which is the object of interest for mass-optimization, has a spanwise width of 4.0 inches, streamwise length of 7.5 inches, and the thickness varies. The high-fidelity finite element model also includes a frame surrounding the panel, which is 0.5 inches thick. The panel and frame together are 5.14 inches wide and 8.64 inches long. That frame sits on top of the wedge and sting mount, which is pointed at the incoming flow. The entire wedge-frame-panel assembly is 5.14 inches wide and 12.14 inches long. The wedge's leading edge forms a 16 degree angle on the underside and is 1 inch thick in total, and 0.5 inches thick where it supports the frame-panel assembly.
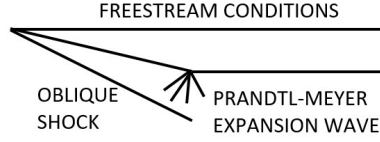
Figure 2: Expected shock structure based on intended experimental wind tunnel setup

2.2 Physical Parameters

The flow conditions used in this analysis represent the conditions experienced in the intended test facility. The stagnation temperature is 540°F, the stagnation pressure is 1800 psia, and the freestream Mach number is 5.85. The material properties of Stainless Steel 17-4PH H900 vary as the temperature varies according to the values reported in the Department of Defense's (DoD) aerospace materials handbook [16].

The expected shock structure over the wedge-frame-panel assembly is shown in Fig. 2, with the flow moving from left to right. When tested, the flow hits the sharp leading edge of the supporting wedge causing oblique shocks to form on the top and bottom surfaces. Because the wedge is positioned at zero degrees angle of attack, the flow turn angle on the top surface is zero degrees, making the oblique shock infinitely weak and allowing the assumption of freestream conditions on the top surface. The flow on the bottom surface turns at a flow turn angle determined from the freestream Mach number and wedge angle, 16 degrees. Using oblique shock aerodynamic theory [17], the pressure is calculated on the top surface where the panel sees the flow and on the bottom surface of the wedge where the cavity is present. The difference between these two pressures is calculated to be 0.0939 psi, which is applied to the computational model as a constant pressure force to represent the steady aerodynamic loading on the thin panel with the given flow conditions.

3 LOW-FIDELITY METHODS

3.1 Equations of Motion

The Equation of Motion and the boundary conditions follow the works of Freydin et al. [6, 13, 18, 19] for a fully clamped plate with first order piston theory fluid forcing and a simple linear thermal stretching term.

$$
M_{ij}\ddot{w}_j + \left(K_{ij} + K_{ij}^A - K_{ij}^{TH} + \tilde{K}_{ij}^{TH_u} + \tilde{K}_{ij}^{TH_v} \right) w_j
$$
$$
+ \left(C_{ij} + C_{ij}^A \right) \dot{w}_j + \left(N_{ijkl}^{(a)} + \tilde{N}_{ijkl}^{(b)} + \tilde{N}_{ijkl}^{(c)} \right) w_j w_k w_l = Q_j \quad (1)
$$

The boundary conditions for a plate clamped on all sides are given:

$$
w|_{x=0}, w|_{y=0}, w|_{x=L_x}, w|_{y=L_y}, \left.\frac{\partial w}{\partial x}\right|_{x=0}, \left.\frac{\partial w}{\partial y}\right|_{y=0}, \left.\frac{\partial w}{\partial x}\right|_{x=L_x}, \left.\frac{\partial w}{\partial y}\right|_{y=L_y} = 0 \quad (2)
$$

Here M is the linear structural mass, C and C^A are the linear structural and aerodynamic damping, K is linear structural stiffness, K^{TH} is the thermal stiffness matrix in the principle component, $\tilde{K}^{TH_u}$ and $\tilde{K}^{TH_v}$ are the thermal stiffness matrices in the in-plane coordinates, and each N term represents the tensile stretching of the plate due to large deflections, i.e. these account

for geometric nonlinearities. Finally, Q_j is a vector of external work done on the system, in this case by static pressure loading.

Writing in matrix form and rearranging slightly, we can write the equation as follows. Here we have combined the thermal stiffness matrices into $\mathbf{K_{TH}}$ and the nonlinear stretching matrices into $\mathbf{N}$. All other terms are simply matrix form representations of the corresponding terms in Eqn. 1.

$$\mathbf{M\ddot{w}} + (\mathbf{C_S} + \mathbf{C_A})\,\mathbf{\dot{w}} + (\mathbf{K_S} + \mathbf{K_A} + \mathbf{K_{TH}})\,\mathbf{w} + \mathbf{N}\mathbf{w}^3 - \mathbf{Q} = 0 \tag{3}$$

For our forthcoming stability analysis used in the optimization, we follow the procedure in [8] to construct an eigenvalue problem from these equations of motion. We can collect terms using $\tilde{\mathbf{q}} = \begin{Bmatrix} \mathbf{q} \\ \mathbf{\dot{q}} \end{Bmatrix}$ to write the equations in state space form.

$$\begin{bmatrix} \mathbf{I} & \mathbf{0} \\ \mathbf{0} & \mathbf{M} \end{bmatrix} \frac{d}{dt}\,(\tilde{\mathbf{q}}) = \begin{bmatrix} \mathbf{0} & \mathbf{I} \\ -\,(\mathbf{K_S} + \mathbf{K_A} + \mathbf{K_{TH}}) & -\,(\mathbf{C_S} + \mathbf{C_A}) \end{bmatrix} \tilde{\mathbf{q}} \tag{4}$$

$$\mathbf{B}\dot{\tilde{\mathbf{q}}} = \mathbf{A}\tilde{\mathbf{q}} \tag{5}$$

Assuming the vector $\tilde{\mathbf{q}}$ has the form $\tilde{\mathbf{q}} = \mathbf{\Psi}e^{\lambda t}$ yields the eigenvalue problem

$$(\mathbf{A} - \lambda_i \mathbf{B})\mathbf{\Psi}_i = 0 \tag{6}$$

Where λ_i and $\mathbf{\Psi_i}$ are the eigenvalue and eigenvector of the ith mode.

3.2 Optimization Statement

The objective is to minimize mass by optimizing the thickness across the plate subject to a flutter and/or buckling constraint, depending on which case (Main Objective 2a–2d) is considered.

The mass is of course a function of the thickness of the plate,

$$\text{mass} = \int_0^{L_x} \int_0^{L_y} \rho h(x,y)\,dx\,dy \tag{7}$$

Where ρ and h are density and thickness, respectively. For this problem we will define the thickness distribution as a summation of thickness mode shapes $\mathbf{\Psi_h}$ and modal coefficients $\mathbf{X}$, which will also be our design variables.

$$h(\mathbf{X}, x, y) = \sum_k X_k \psi_k(x,y) = \mathbf{\Psi_h}\mathbf{X} \tag{8}$$

As it will be shown, this enables relatively few design variables to represent relatively complex panel designs as opposed to discretizing the entire area of the plate and assigning each discretization point a thickness design variable. In addition, it enables analytic differentiation desired for efficient gradient-based optimization. The tradeoff is that the engineer is left with the choice of a modal basis for $\mathbf{\Psi_h}$. For this case, we employ up to nineteen modes, the first three being $\Psi_1 = 1$, $\Psi_2 = x$, and $\Psi_3 = y$, followed by the first four modes for a clamped-clamped

beam, cross multiplied to generate sixteen plate modes. In this manner, we can compare a one-design variable solution as the baseline uniform thickness solution to a host of other solutions with only 19 variables, whereas discretizing the plate into even a relatively coarse mesh would increase the size of the problem considerably, with the problem scaling with n^2.

The buckling and flutter constraints are accounted for by considering linear frequencies computed by Eqn. 6. The frequency value for any mode i is defined by the imaginary part of its eigenvalue, $Im(\lambda_i)$. Buckling occurs when any frequency value becomes zero—there is no structural stiffness remaining. Similarly, the damping value for any mode i is defined by the real part of its eigenvalue, $Re(\lambda_i)$, and flutter occurs when any damping value crosses zero. Therefore, we solve for each eigenvalue at each iteration to determine stability.

For the buckling optimization problem, no piston theory aerodynamics are applied as it is assumed that linear buckling will be mainly driven by thermal stiffness ($\mathbf{K_{TH}}$ in Eqn. 4) rather than aerodynamic terms at low initial deflections. The optimization problem statement with a buckling constraint and minimum thickness constraint can be written as follows:

$$
\begin{aligned}
\text{minimize} \quad & \text{mass}(X_k) \\
\text{by varying} \quad & X_{k,min} \leq X_k \leq X_{k,max} && k = 1, 2, ...n_k \\
\text{subject to} \quad & Im(\lambda_i(M_\infty, T_0)) < 0 && i = 1, 2, ...n_i \\
& h > h_{min} \\
& M_\infty = 5.9 \\
& T_0 = 555K
\end{aligned}
\tag{9}
$$

Where n_k is the chosen number of thickness mode shapes (and therefore design variables) and n_i is the chosen number of structural mode shapes. For this study, nine structural mode shapes were found to be sufficient in achieving modal convergence for cases with 12 design variables.

The optimization problem statement with a flutter constraint and minimum thickness constraint can be written as follows:

$$
\begin{aligned}
\text{minimize} \quad & \text{mass}(X_k) \\
\text{by varying} \quad & X_{k,min} \leq X_k \leq X_{k,max} && k = 1, 2, ...n_k \\
\text{subject to} \quad & Re(\lambda_i(M_\infty, T_0)) < 0 && i = 1, 2, ...n_i \\
& h > h_{min} \\
& M_\infty = 5.9 \\
& T_0 = 555K \\
& 5.5e6Pa \leq P_0 \leq 10e6Pa
\end{aligned}
\tag{10}
$$

In this case, aerodynamic terms are included with a range of total pressures to prevent hump modes, where at the desired $P_0 = 10MPa$ the flutter constraint is met, but in lower pressures, there is an instability. Also, because flutter will occur well after thermal buckling, the flutter constraint must be solved at a statically buckled nonlinear equilibrium point. Details on performing a linear dynamic analysis around a static nonlinear solution appear in [19]. One conclusion can be drawn from this immediately that to allow a panel to buckle but not flutter is to allow a much less conservative design while still retaining dynamic stability.

3.3 Sensitivities

To enable gradient-based optimization, the derivatives of the objective function and constraint functions are required. The modal method presented here is a good candidate for analytical derivatives, since the functions are known and in most cases are simple. However, when analytic gradients are not available, the solution method implemented as described in Sec. 3.4 permits finite difference gradient calculation.

The gradient of our objective function mass (Eqn. 7) with respect to the design variable X_k is given by:

$$\frac{d(\text{mass})}{dX_k} = \frac{\partial}{\partial X_k} \int_0^{L_x} \int_0^{L_y} \rho h(X_k, x, y) \, dx \, dy = \int_0^{L_x} \int_0^{L_y} \frac{\partial}{\partial X_k} \rho \sum_k X_k \psi_k(x, y) \, dx$$

$$= \int_0^{L_x} \int_0^{L_y} \rho \psi_k(x, y) \, dx \quad (11)$$

The gradient of the thickness with respect to the design variables for use in the minimum thickness constraint is given by:

$$\frac{dh}{d\mathbf{X}} = \mathbf{\Psi_h} \tag{12}$$

The gradients of the eigenvalue constraints are available to analytically differentiate as shown in [8, 12, 20], however in this work the finite difference method was implemented.

3.4 Numerical Implementation

The computational code is written in Python and the optimization is performed with SciPy's optimization library using the Sequential Least Squares Programming (SLSQP) method. For each case, several initial design variable values were seeded as initial conditions to the optimizer, but no formal design space sampling method such as a Latin hypercube was implemented. Because SLSQP is a gradient-based solver, this does permit the possibility of finding a local minimum and missing the global minimum. Care was taken to identify what appeared to be a global minimum. The built-in finite differencing algorithm was used for gradient calculations of any terms not given as analytical gradients. All cases run on a laptop on the order of seconds.

4 HIGH-FIDELITY METHODS

A Finite Element Analysis (FEA) model of the wedge-frame-panel assembly described in Section II is created in ABAQUS to support the in-house code. The goal is to perform a two-step aerothermoelastic analysis to find a baseline panel thickness with a higher degree of fidelity than the in-house optimization model.

This analysis is separated into two steps because with a thin geometry such as these panels, FEA can be run with different types of elements to reduce computational cost while retaining accuracy. Solid elements must be used for Step I because shell elements in ABAQUS cannot be used in heat transfer analyses. However, shell elements will be cheaper if applicable.

Table 1: Comparison of computational cost for isolated panel, frame-panel, and wedge-frame-panel assemblies

Model Type	Number of Elements	Number of Nodes
Isolated Panel	3,000	3,116
Frame-Panel	12,144	15,332
Wedge-Frame-Panel	44,180	54,059

Table 2: Frequency comparison (in Hz) for different approximate models of simplified panel

Mode #	1	2	3	4	5	6
Isolated Panel	367.74	492.84	714.51	950.41	1030.5	1070.6
Frame-Panel	360.26	484.23	703.67	930.18	1016.2	1049.2

To compare the computational cost of each model, the number of elements and nodes are shown in Table 1. This compares the isolated panel, the frame-panel assembly, and the wedge-frame-panel assembly (used in Step I). Table 2 shows that the natural frequencies for the isolated shell panel model with clamped boundary conditions nearly match the solid frame model. Therefore, since the frame-panel model has over four times the elements than the isolated panel but the frequencies are in satisfactory agreement, it can be concluded that the model with clamped boundary conditions simulating the frame provides a computational simplification without sacrificing the accuracy of the results.

The process outlined below is run on several constant thickness panels to determine the minimum constant thickness panel (least amount of mass) that meets the required factors of safety of the intended test facility, Wright-Patterson AFB's Mach 6 High Reynolds Facility (M6HRF). The required factors of safety for M6HRF are 3 and 4 for the yield strength and ultimate strength, respectively. This constant thickness panel is then used as the baseline panel in the optimization methods.

4.1 Step I

The first step of this two-step process is a high-fidelity three-dimensional aerothermodynamic transient solution. The entire wedge-frame-panel assembly is used, and has three-dimensional heat transfer elements. A heat flux distribution is approximated based on the Eckert Reference Enthalpy Method [21] and turbulent flow is assumed. Eq. 13 solves for the reference enthalpy of a boundary layer and the heat flux distribution across each surface is approximated using Eq. 14 with the flow properties being evaluated at the reference condition determined by Eq. 13 [21].

$$H^* = 0.5(H_e + H_w) + 0.22(H_e r \frac{\gamma - 1)}{2} M_e^2 \tag{13}$$

$$Q(x) = St^* \rho^* V_e (H_{aw} - H_w) \tag{14}$$

These equations solve for the heat flux distribution across each respective surface on the assembly. Each heat flux distribution is applied as a temperature field in ABAQUS. A predefined temperature field of 75°F is set, accounting for room temperature of the tunnel. A transient heat transfer analysis is run for 30 seconds, the assumed time for wind tunnel entry. The resulting
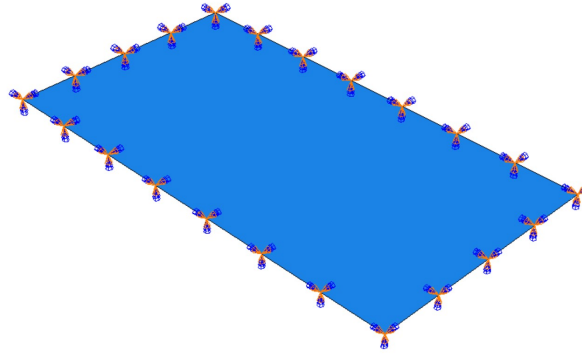
Figure 3: Simplified panel model with clamped boundary conditions representing the frame

temperature distribution over the top of the panel after 30 seconds is saved for each run and used in Step II.

4.2 Step II

The second step is a nonlinear aerothermoelastic static stress analysis on a simplified shell panel model, shown in Fig. 3.

Because the thin panel heats up much quicker than the thicker frame, the temperature difference between points on the panel and the temperature of the frame drive the thermal buckling of the panel. Therefore, the clamped boundary conditions are held at a constant temperature. This temperature is chosen to be the average frame temperature from the results of the first step. The panel's temperature distribution is mapped over from each node of the three-dimensional model in Step I and applied as a temperature field in Step II. The pressure force is the resulting pressure force from aerodynamic oblique shock theory, as detailed previously. This pressure force is assumed to be at a constant value of 0.0939 psi applied across the top surface of the panel. It should be noted that this is not a coupled analysis, meaning that the thermal and pressure loads are not being updated after stress and deflection are calculated for each thickness. Von Mises stresses from the applied thermal and pressure loads are used to evaluate the failure of the panel.

5 RESULTS

5.1 Baseline Uniform Thickness Panel

As a point of comparison for the variable thickness optimized panels, we first design a baseline panel with uniform thickness that satisfies the experimental facility's factor of safety requirements. During this process, significant physical insight was gained into how the nonlinear coupled physics drive this design; thickness drives temperature and stress in a very nonlinear fashion.

The relationship between thickness and temperature is fundamental to this analysis. An example of the resulting temperature contours after Step I for the 0.075 inch panel is shown in Fig. 4. All panel thermal distributions have generally the same contours with varying magnitudes, which depends on thickness. This is represented by Fig. 5, which plots the maximum temperature found on the panel for each thickness. The maximum temperature on the panel decreases monotonically as the thickness increases—an expected result since a thinner surface would tend to heat up quicker than a thicker one. This plot also shows the average temperature of the frame surrounding the panel. The frame temperature remains nearly constant, which is also expected since the frame thickness and heat loads being applied do not change as panel thickness varies.
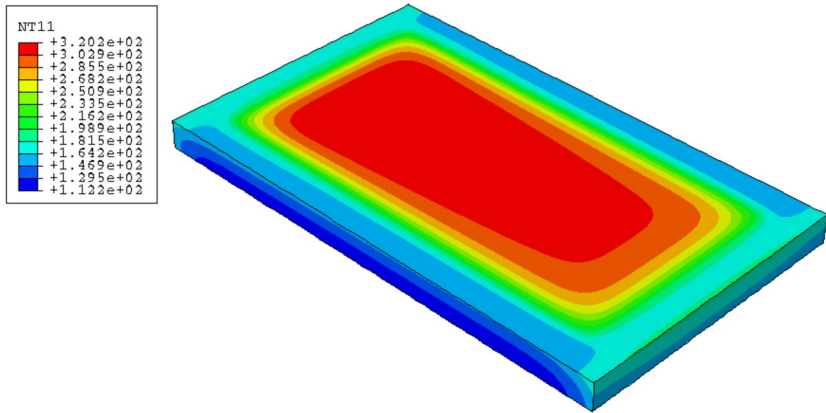
Figure 4: Temperature distribution (in °F) on 0.075 inch panel from Step I transient heat transfer analysis after 30 seconds
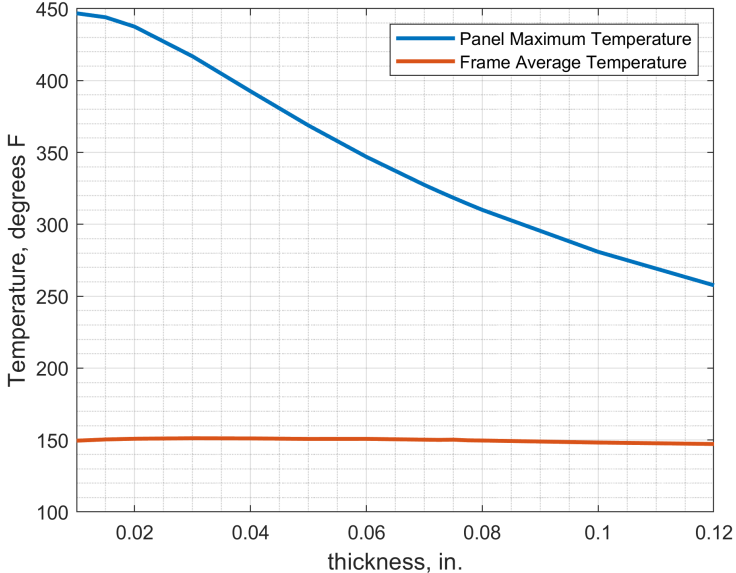

Figure 5: Temperature difference between maximum temperature measured on panel and average temperature of frame
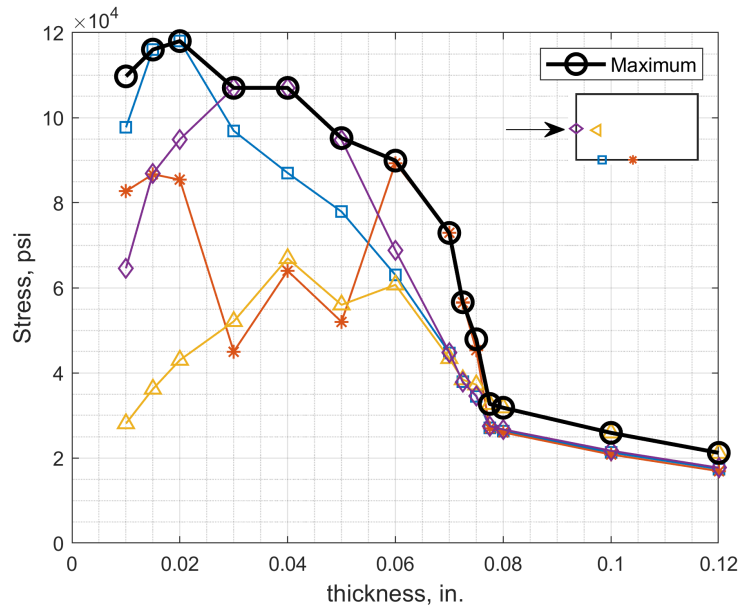
Figure 6: Stress measured at different locations on the panel, shown in the legend with flow direction, and maximum stress anywhere on panel
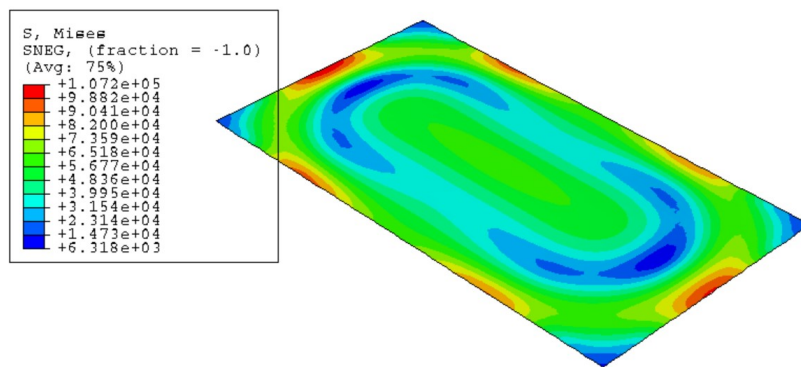

Figure 7: Stress distribution (in psi) for panel thickness 0.04 inches

The panel stresses from Step II are considered next. The panel stresses are critical to this analysis since the maximum stress is ultimately used to calculate the factor of safety for each thickness, which drives the baseline panel design. Fig. 6 plots stress at four different locations on the panel as well as the maximum found at any location on the panel. Maximum stress increases as thickness increases for extremely thin panels. Deaton [9] had similar findings in his study on the effects of geometric nonlinearities on structures with heat loads. Essentially, thermal expansion from the heat loads causes compressive stresses that load the panel in the opposite direction of the nonlinear tensile stretching for extremely thin panels. Eventually, this effect cancels, and the maximum stress decreases as panel thickness increases. The location of maximum stress and stress distributions both vary with thickness, which is why several locations are chosen for tracking stresses. These locations are referenced in the legend of Fig. 6 with a top-view of the panel indicating the flow direction. There is a clear difference in the stress distributions for thicker panels versus thinner panels, with a transition point occurring at the 0.0775 inch panel. Figs. 7 and 8 show the general stress distribution for panels thinner and thicker than the 0.0775 inch panel, respectively.

The out-of-plane displacement has an interesting correlation with the stresses found in different
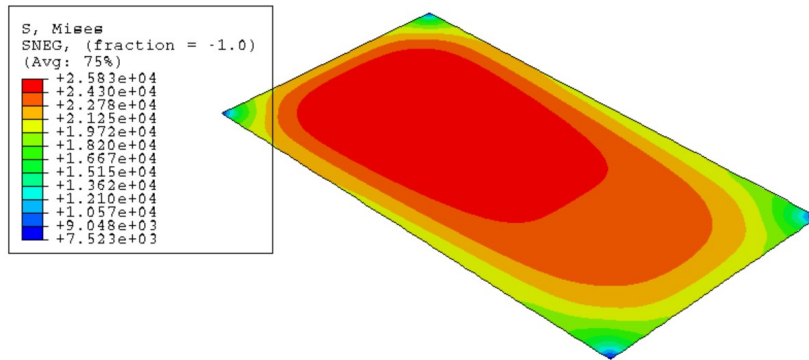
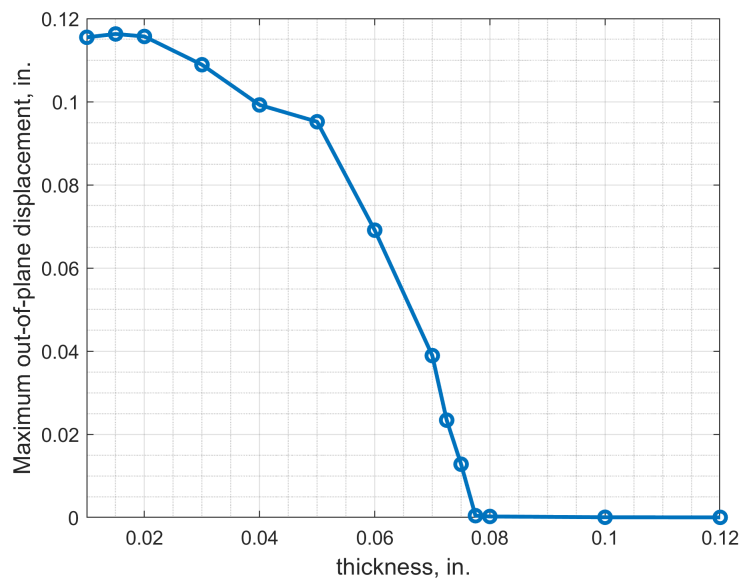Figure 8: Stress distribution (in psi) for panel thickness 0.1 inches

Figure 9: Out-of-plane displacement as thickness varies

panel thicknesses. Fig. 9 shows the relationship between the maximum out-of-plane displacement and panel thickness. It is to be noted that the out-of-plane displacement decreases as panel thickness increases and decreases by two orders of magnitude at a panel thickness of 0.0775 inches, which is the same point at which the stress distributions undergo a drastic change and the relationship between stress and thickness becomes linear. This indicates that the panel is buckled when thinner than 0.0775 inches since the stresses are mainly curvature based, and not buckled when thicker than 0.0775 inches since the stresses are mainly compressive.

A thermal buckling analysis is performed on a 0.03 inch panel to confirm that the panels thinner than 0.075 inches are in fact buckled. Fig. 10 shows how the first natural frequency and maximum out-of-plane displacements change as the thermal loading is increased. The frame temperature is held at a constant temperature of 150°F while the panel temperature is increased incrementally. The panel temperature is one uniform temperature in this case, not a distribution like the aerothermoelastic analysis requires. The temperatures in the plot represent the temperature difference between the frame and the temperature being applied to the panel. It can be seen that the first natural frequency reaches a minimum point at about a 23°F temperature difference, which is also the point where the maximum displacements begin to increase more rapidly, indicating unstable buckling [22].
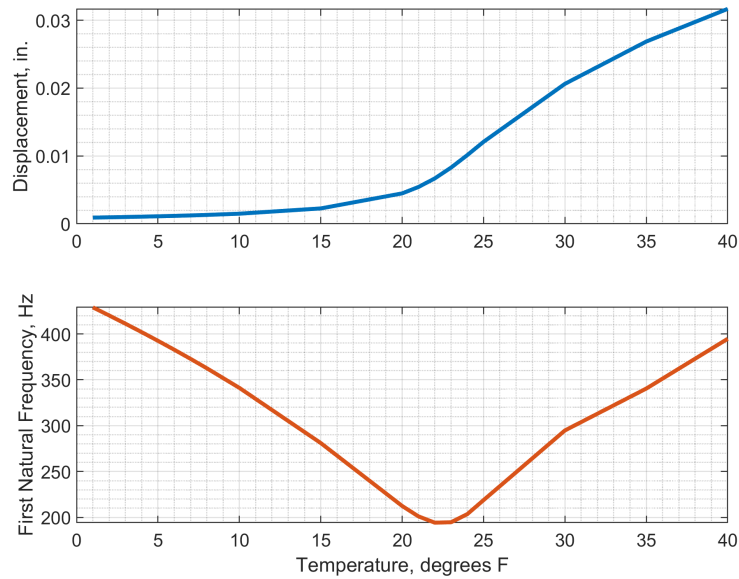
12

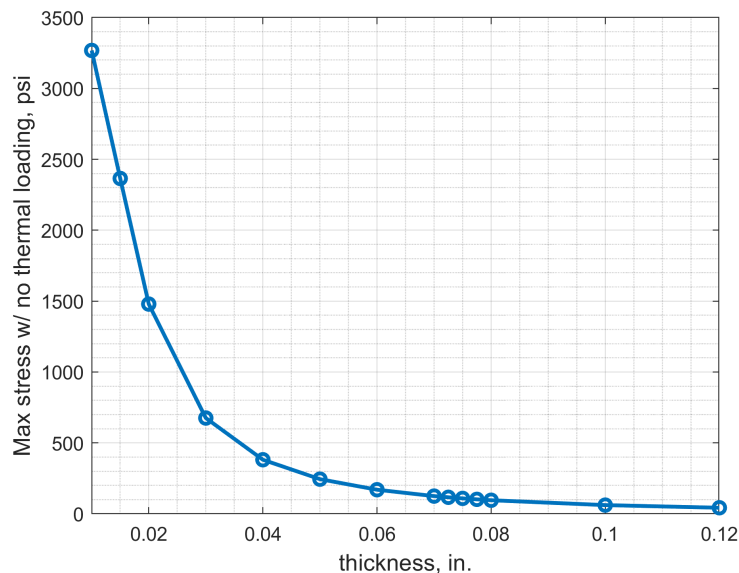Figure 10: Thermal buckling of 0.03 inch panel

Figure 11: Max stress vs. thickness for clamped panel with no thermal loading

To further explore the effects of the thermal loading on panel buckling, a stress and displacement analysis is performed for the same range of panel thicknesses as the aerothermoelastic analysis, but this time omitting the thermal loads so that there is only aerodynamic loading (here, a constant pressure force). A static stress analysis is done for a clamped panel with a pressure load of 0.0939 psi. The resulting maximum stress and maximum displacement graphs are shown in Figs. 11 and 12, respectively. Both maximum stress and displacement decrease monotonically and nonlinearly as panel thickness increases for this purely mechanically loaded system. These results also confirm the argument posed by Deaton [9] as to why the panel's maximum stress increases as thickness increases first, then decreases; thermals drive the thin panel stress problem.

Although the stress distributions vary quite a bit as panel thickness varies, it is still important to determine the factor of safety for each thickness using the maximum stress on the panel, regardless of the location where that occurs. This is to ensure safety in the wind tunnel for
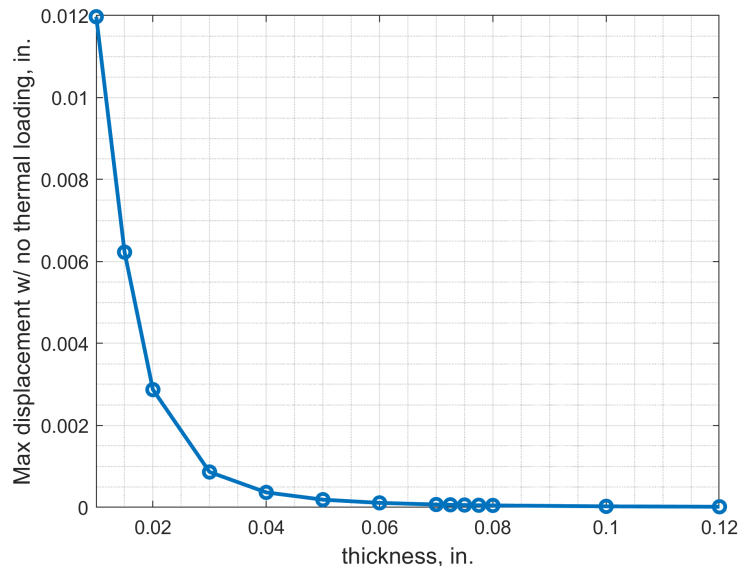
Figure 12: Max displacement vs. thickness for clamped panel with no thermal loading

future experimental testing. The factors of safety are determined using the yield and ultimate strengths of Stainless Steel 17-4PH H900 sheet, strip, or plate condition, which are temperature-dependent [16]. The yield and ultimate strengths are calculated based on the maximum temperature recorded on the panel in Fig. 5 for each thickness. The factors of safety are then calculated by dividing the yield and ultimate strength by the maximum stress for each panel thickness. Fig. 13 shows the relationship between panel thickness and factor of safety for both the yield and ultimate strength.

It is determined that the minimum required thickness to meet the required factors of safety of the intended experimental facility, M6HRF, is 0.075 inches, which becomes the baseline constant thickness panel, Panel A in Table 3. The stress distribution for this panel is shown in Fig. 14.

5.2 Validation of In-House Analysis Tool

To validate the in-house modal solution against the Abaqus analysis, the maximum out-of-plane displacement for each thickness subjected to a temperature difference from Fig. 5 is calculated using the in-house code. Fig 15 compares these solutions to the corresponding Abaqus solutions, which show excellent agreement. Discrepancies exist at thinner plates because the Abaqus solution includes the non-symmetric heat soak from the Eckert's Reference enthalpy method described in Sec. 4.1, whereas the in-house model considers a uniform thermal field. Therefore, a comparison of displacements at the midpoint may be preferred over the current maximum displacement validation method, but the results are clear that the method is viable. Indeed, the bifurcation point at a thickness of 0.0775 inches is in remarkable agreement regardless of the displacement magnitude.

The same thermal buckling analysis done in Abaqus (Fig. 10) is also done with the in-house code for a 0.03 inch constant thickness panel swept through temperatures to confirm agreement between methods. Figure 16 compares the thermal buckling results for these two methods and show close agreement on both displacement and frequency per temperature difference. The displacement plot shows that our method may be more stiff in the post-buckled regime than Abaqus.
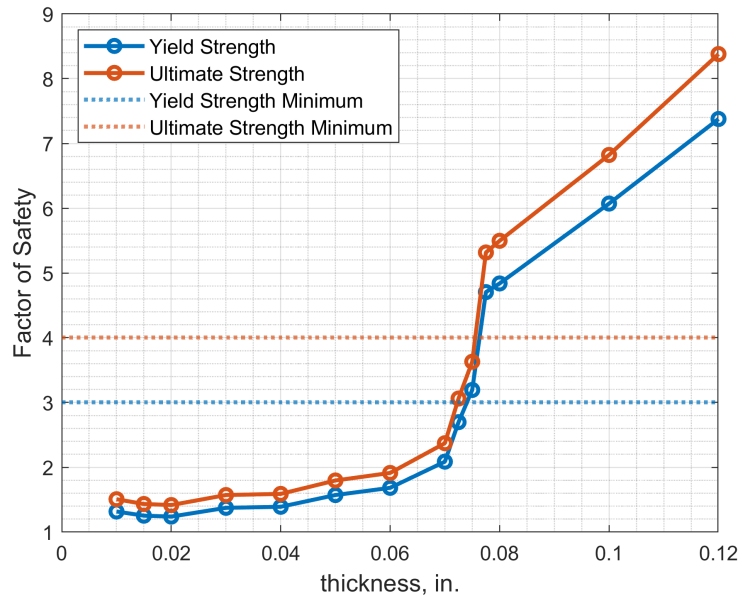
14

Figure 13: Factors of safety of maximum stress measured on panel versus minimum required factors of safety for M6HRF
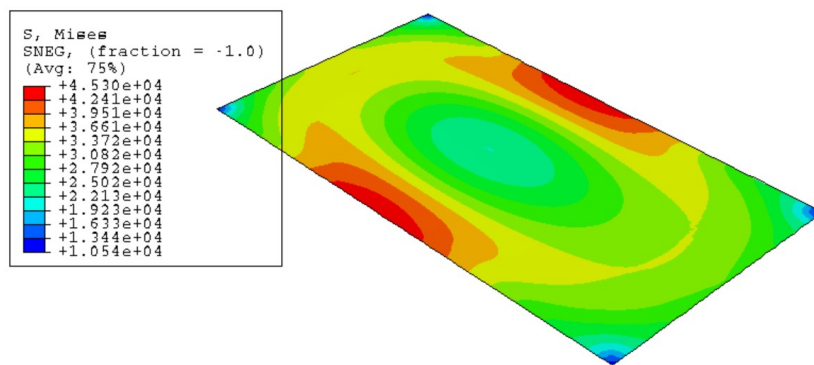

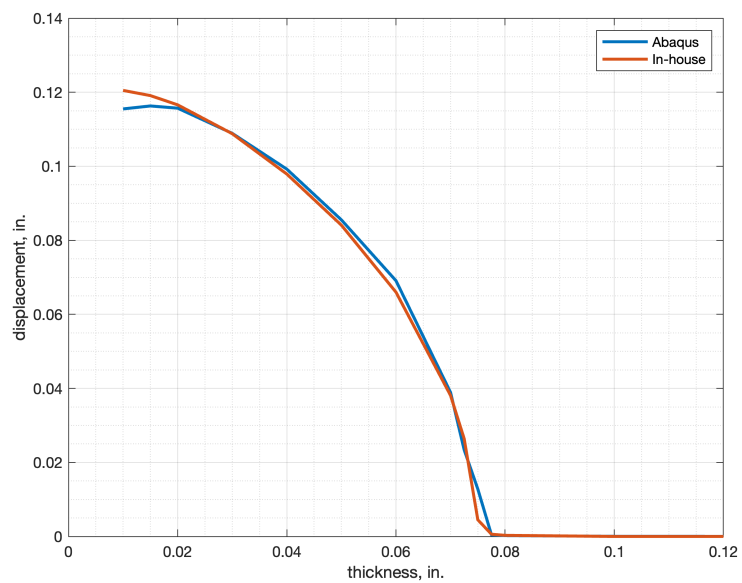Figure 14: Stress distribution (in psi) for panel A, thickness 0.075 inches

Figure 15: Displacement versus thickness comparison for Abaqus and in-house modal methods
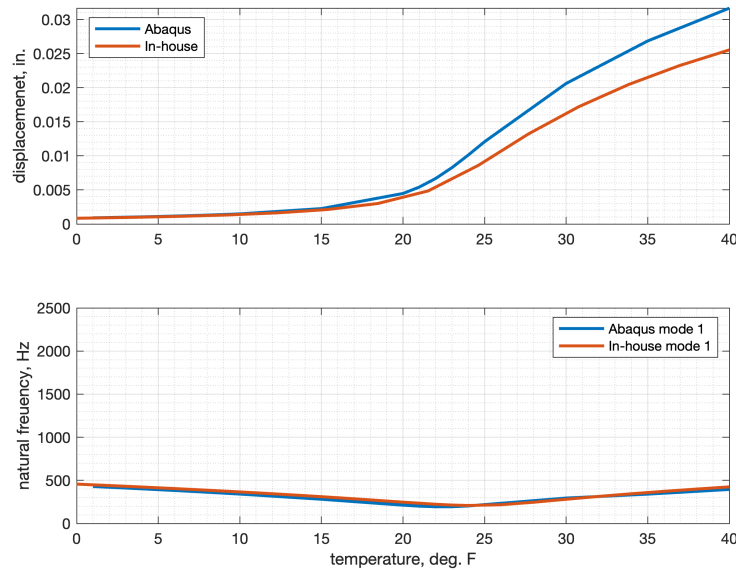
Figure 16: Thermal buckling comparison for Abaqus and in-house modal methods for 0.03 inch panel

5.3 Optimizing Thickness for Buckling

The in-house modal method is used with 3 modes in streamwise deflection, 3 in spanwise deflection, and 12 thickness modes to generate a variable thickness geometry which minimizes weight but does not buckle. A uniform temperature differential from frame to panel is applied in accordance with Fig. 5, but no aerodynamics are used for the buckling case, since the thermal effects dominate the problem compared to aerodynamic effects. The uniform thermal distribution results in an axisymmetric distribution of thickness, whereas the true thermal distribution is not uniform and would most likely result in an asymmetry along the streamwise direction. The resultant geometry is exported to Abaqus and shown in Fig. 17a. The center of the panel is the thickest, decreasing in thickness moving outward, and then increasing again before meeting the boundaries. The thickness distribution prioritizes material in areas of high curvature due to buckling, and low thickness in areas with less curvature. Indeed, the thickness distribution is reminiscent of the second derivative of the first buckled mode shape.

Once the design is optimized using the in-house code, the same two-step aerothermoelastic process outlined in Sec. 4 is used to validate that the in-house code's analysis against higher fidelity analysis tools. Step I of this process is a heat transfer analysis on the 3D solid model. To create a variable thickness 3D model in Abaqus, splines are created spanwise and streamwise to extrude the approximate variable thickness distribution as output by the in-house code. The resulting temperature distribution is directly applied to the shell model for Step II, in which the thickness coordinates optimized by the in-house code are directly applied as a shell thickness distribution (Fig. 17a). The temperature distribution is shown in Fig. 17b. Note that because the thermal flux is applied from the Eckert's reference enthalpy technique, the thermals are now asymmetric with the flow and the upstream side of the panel reaches a higher temperature than downstream. The resulting stress distribution is shown in Fig. 17c, indicating a similar increase in stress where the plate is hotter. Finally the vertical displacement is shown in Fig. 17d, again showing the effects of asymmetric heating with the upstream side of the panel displacing more than the downstream side. However, the displacement is several orders lower than the thickness of the panel, confirming that the panel is in an unbuckled state. The mass of this panel is reported as Panel B in Table 3. Note that this variable thickness panel is 6.61% lighter than the minimum uniform thickness panel when subjected to the same buckling constraint.
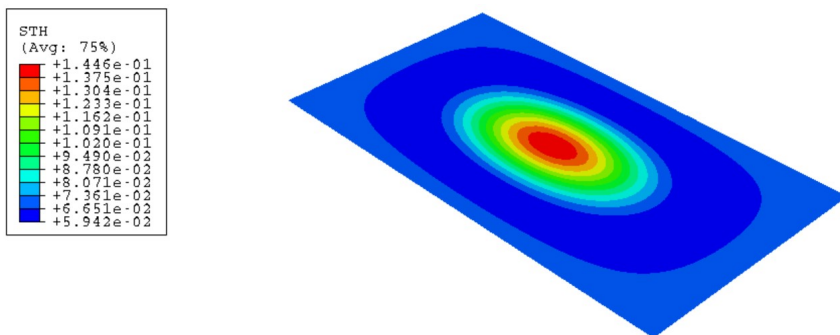
(a) Thickness distribution
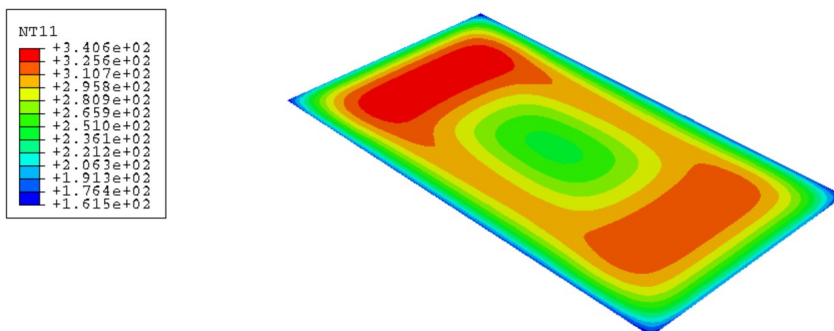
(b) Temperature distribution

(c) Stress distribution

(d) Out of plane displacement

Figure 17: Panel B results: the unbuckled panel thickness distribution and resulting temperature, stress, and displacement when subjected to aerothermal heating
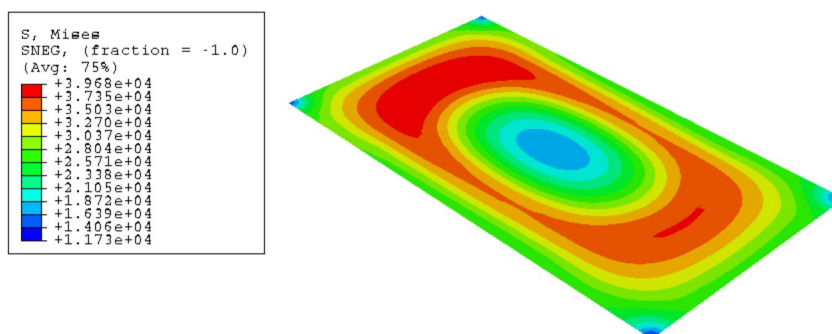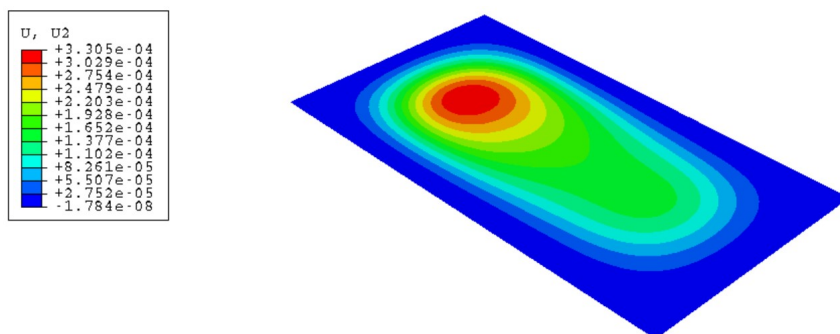
(a) Thickness distribution

(b) Temperature distribution
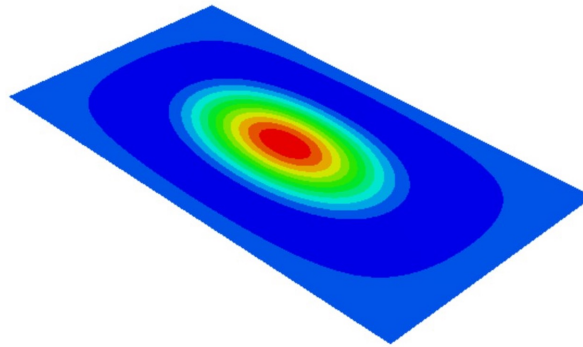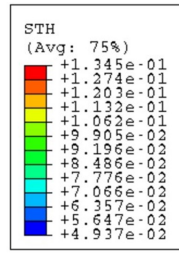

(c) Stress distribution
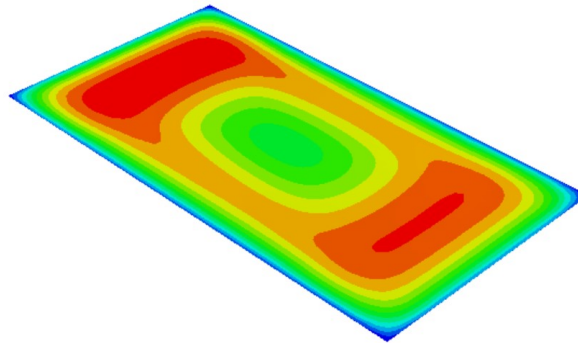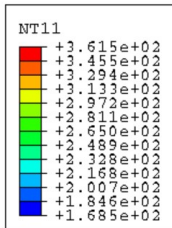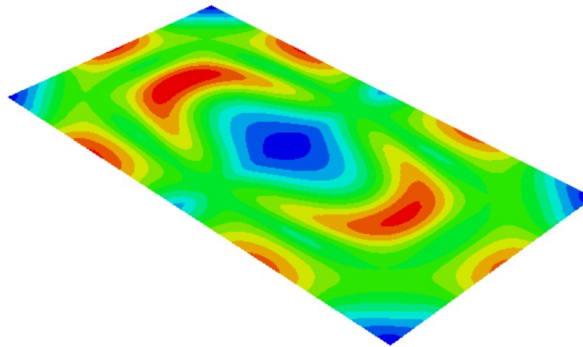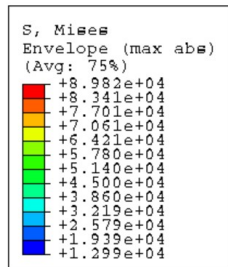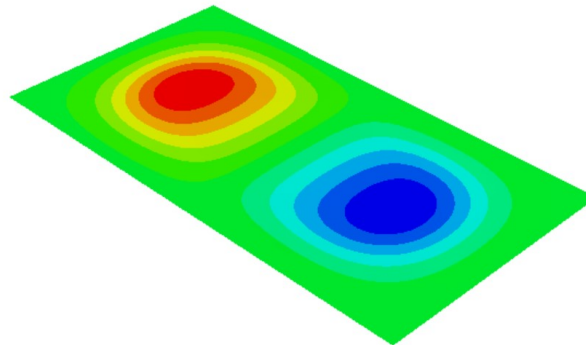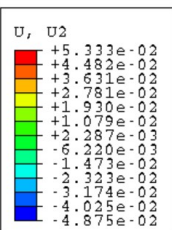

(d) Out of plane displacement

Figure 18: Panel C: the buckled panel thickness distribution and resulting temperature, stress, and displacement when subjected to aerothermal heating

Table 3: Mass and savings for optimum thickness panels

	Not Buckled	Lightly Buckled	No Flutter	LCO
Constant thickness mass [kg]	0.2995	0.2893 A	0.0469* D	E
Variable thickness mass [kg]	0.2797 B	0.2402 C	F	G
Mass Savings [%]	6.61	16.97		

To compare to the baseline Panel A, which is very lightly buckled, the constraint in Eqn. 9 must be relaxed. To do so, an ad-hoc design study is performed in which uniform thickness is simply removed from Panel B until the panel buckles. The goal with this comparison is to show similar qualitative structural behavior, ie light buckling, at a lower mass. The buckled panel, shown in Fig. 18a, is created in Abaqus by subtracting 0.01 inches from each thickness point so that the distribution remains the same but the magnitude changes. The displacement is on the order of magnitude of the buckled constant thickness panels, indicating a lightly buckled panel, and the stress is at its maximum on the edges, just as it was for the buckled constant thickness panels. The resulting temperature, stress, and displacement distributions are shown in Figs. 18b, 18c, and 18d, respectively. The temperature distribution is similar to the thicker Panel A, but the stress distribution is quite different, owing to the mode 2 buckled deflection of the panel under these conditions. The mass of this panel is given as Panel C in Table 3. Note that this Panel C is 17% lighter than Panel A which has a similar lightly buckled status.

5.4 Optimizing Thickness for Flutter

To incorporate the flutter constraint, the optimization in Eqn. 10 is performed for a flat plate. Because we are no longer monitoring the static buckling characteristics but only dynamic flutter events, no thermals are applied. The mass result is given for Panel D in Table 3. Immediately it is seen that by ignoring buckling—in effect allowing the plate to buckle—the weight is drastically reduced by over an order of magnitude between the unbuckled flat panel and the flutter-free flat panel. Further work will generate an optimized variable thickness panel with flutter considerations, Panel F, to compare with the flat Panel D at this condition. However before this is attempted, let us address a few subtleties.

5.5 A Discussion on How Nonlinear Aerothermoelastic Physics Affects the Design Space

When including both aerodynamic flutter and thermoelastic buckling constraints, the optimizer has difficulty converging to a solution. To gain insight into why, the problem space must be further understood. To do so, we draw a contour plot, Fig. 19, reminiscent of that in Dowell's early work [1]. Here, λ is the ratio of aerodynamic to structural stiffness and R_x is the ratio of thermal to structural stiffness. The contour plot shows the root mean square (rms) of a point at the quarter-chord, quarter-span of the plate. This plot is generated for a range of panel thicknesses from 0.01-0.1 inches, and temperature differentials up to 70K, which is the highest Riley [15] reports in tunnel experiments.[1]

In the bottom left corner, at the origin, the plate is at zero loading and thus is at zero dynamic behavior. Increasing along the positive x-axis increases thermal loading until the plate buckles at an R_x/π^2 value of around 11. Increasing from the origin up the positive y-axis increases the

---

[1]Future work will repeat Section 5.3 with this consideration, namely that the aerothermal heating analysis described in this work results in much larger temperature differentials than what is seen in practice in tunnel experiments.
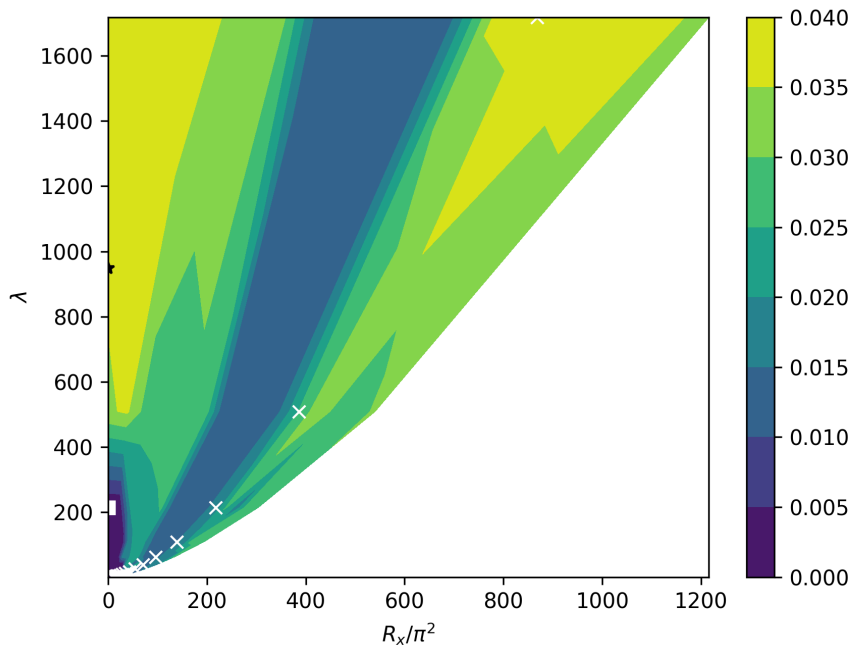
Figure 19: Contour plot detailing the effects of aerodynamic stiffness λ on the y axis and the thermal stiffness ratio R_x/π^2 on the x axis. The color contour is the root mean square of a point on the plate at the quarter-chord and quarter-span location. Contour is in inches.

aerodynamic effect on the panel until the panel flutters, at $\lambda = 214$. This point is marked with a white square.

The result given for Panel D in Table 3 is that of zero thermal gradient, and therefore from Fig. 19 we should expect the optimizer to find the thinnest stable panel along the y axis, ie the white square. However, the optimizer does not find this point. It instead finds the point marked with the black star, at $\lambda = 949$. How can this be?

Owing to the third order structural nonlinearity, the bifurcation is subcritical and has up to three solutions. Figure 20 shows that for a larger initial condition, the solution reaches a stable LCO at a lower λ value of around 250, and for a smaller initial condition, the system remains at a stable undeflected state until nearly $\lambda = 1000$. This discrepancy points out two complexities in the results as presented here. First, the contour plot in Fig. 19 was computed from larger initial values, and thus is more conservative than one generated from smaller initial values (to be presented in future work). Second, the linear flutter solution sought by the optimizer via Eqn. 10 is the less conservative linear solution. The more conservative solution results in a plate mass of 0.07700kg, considerably larger than the mass of Panel D.

Consider now both aerodynamic and thermal effects. If we look at the top left corner, where the plate is under no thermal stress but is experiencing an aeroelastic LCO, and move rightward by increasing the thermal stress, something interesting occurs. The rms amplitude decreases and at some point, the plate buckles and the dynamics stop. That is, the buckling stress is enough to overcome the aeroelastic dynamics and bring the plate to a statically stable but nonlinearly deformed state. This is the behavior depicted by the blue streak running between two patches of light green. Increasing thermal gradients brings us to the next patch of green, where the dynamics begin again. However, there does not seem to be a guarantee that the dynamics are
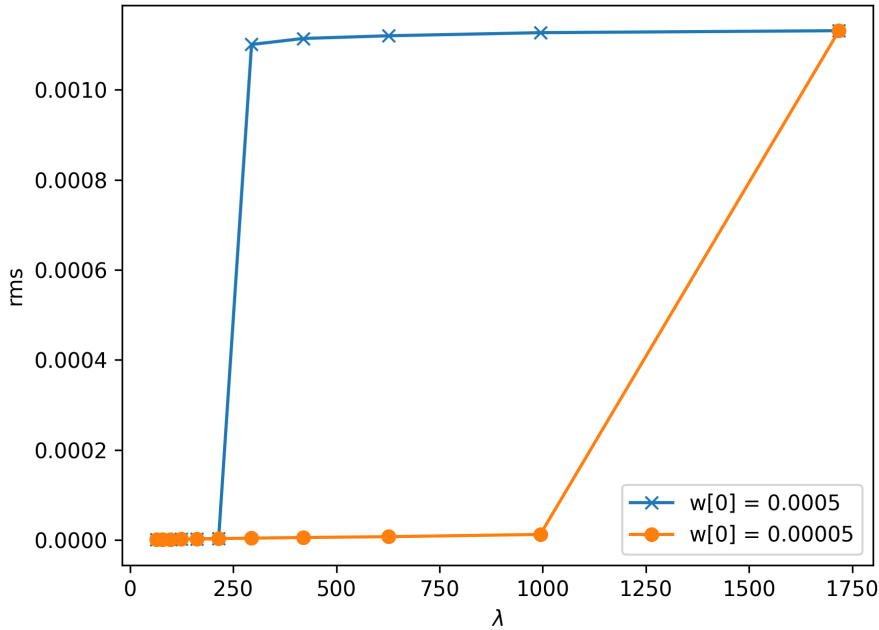
Figure 20: Depending on initial conditions $w[0]$, there are three solutions. The two stable solutions are plotted here, illustrating a subcritical bifurcation.

of the same type, per se. For example the flutter mode in the top left is a merging of the first and third (streamwise) modes, but the flutter mode in the top right depends on the cavity pressure, and may be a merging of first and third or second (spanwise) and fourth (streamwise and spanwise) modes. This appears to be a secondary bifurcation, strong enough to reintroduce dynamics.

Another path to follow is via the the white x's, which depict a simple "optimization trajectory." In the top right is a white x at about $(800, 1500)$ representing a thin panel at a temperature differential of 50K. Keeping the temperature differential the same but increasing panel thickness results in a drop in both aerodynamic and thermal stiffness effects, and we can follow the x's down and left. The trajectory begins within the green dynamically stable LCO region, but as thickness increases, the trajectory falls within the blue statically stable buckled region. Increasing thickness further, the trajectory finally ends in the dark blue undeformed region. It is possible to imagine a similar trajectory shifted upwards that cuts across all four distinct regions of the plot. So, it is difficult—or rather impossible—to rely on our simplistic linear stability bounds based on the linear eigenvalue approach. To more appropriately tackle the problem, a solution is needed where the system's static and dynamic stability is characterized about its nonlinear state, and this behavior is fed to the optimizer as a constraint. This is the direction of future work.

6 CONCLUSIONS

This work demonstrates the initial results of a weight-minimization technique for the design of aeroelastic panels constrained by panel flutter and thermal buckling. Using the Galerkin method to build a modal model of the plate and to build a thickness distribution, the method presented is a computationally-efficient option for optimization, with few design variables able to realize complex designs. Python's SciPy.optimize library is used to perform gradient-based

21

optimization with eigenvalue and thickness constraints. Results indicate potential for weight reduction on the order of 6-17% compared to flat panel designs.

The objectives 1, 2b-c, 3, and 4a-b set forth in the introduction are met. The utility of low-fidelity modeling in this design sense is clear: the aerothermoelastic modeling at this fidelity allows for efficient exploration of stability in this design space. The use of the modal thickness design variables enables complex shapes with relatively few design variables. Buckling constrained optimization was successful for variable thickness and uniform thickness plates. A flutter-free flat plate was designed and variable thickness plates need to be addressed as a future point of comparison. It is anticipated that a similar or larger weight offset will occur for flutter-free plates as they did for buckling-free plates. The high fidelity analysis tools in Abaqus were shown to successfully augment and validate the in-house modal code. Finally, each design case was chosen with objective 4 in mind, the experimental campaign. Panel A, B, and C were chosen definitively to be tested. Flutter cases are yet to be determined, but a discussion of the coupled nonlinear aerotheroelastic physics aids in the understanding of how to design for these cases.

Directions for further future work include: rewriting the optimization statements to consider nonlinear stability behavior; comparing the panel thickness design masses presented here to the masses of typical stiffened panels with traditional hat stiffeners; expanding to curved or otherwise higher-complexity panel geometries. This final idea is an extension of the current method which would require the computation of the mode shapes and frequencies of the new panels, and then assigning thickness mode shapes, but the overall methodology remains the same.

ACKNOWLEDGMENTS

7 REFERENCES

[1] Dowell, E. H. (1970). Panel flutter: A review of the aeroelastic stability of plates and shells. *AIAA Journal*, 8(3), 385–399. ISSN 00011452. doi:10.2514/3.5680.

[2] Mei, C., Abdel-Motagaly, K., and Chen, R. (1999). Review of nonlinear panel flutter at supersonic and hypersonic speeds. *Applied Mechanics Reviews*, 52(10), 321–332. ISSN 00036900. doi:10.1115/1.3098919.

[3] Spottswood, S. M., Beberniss, T. J., Eason, T. G., et al. (2019). Exploring the response of a thin, flexible panel to shock-turbulent boundary-layer interactions. *Journal of Sound and Vibration*, 443, 74–89. ISSN 10958568. doi:10.1016/j.jsv.2018.11.035.

[4] Riley, Z. B., Perez, R. A., and Ehrhardt, D. A. (2021). Response of a Thin Panel to Aerothermal Loading at Mach 6. *AIAA Journal*, 59(9), 3787–3793. ISSN 0001-1452. doi:10.2514/1.j060404.

[5] Brouwer, K. R., Solutions, A. T., Ehrhardt, D. A., et al. (2021). Fluid-Structure Interaction on a Thin Panel Including Shock Impingement Effects. *AIAA Scitech 2021 Forum*, (January), 1–22. doi:10.2514/6.2021-0910.

[6] Freydin, M., Dowell, E. H., Spottswood, S. M., et al. (2020). Nonlinear dynamics and flutter of plate and cavity in response to supersonic wind tunnel start. *Nonlinear Dynamics*, (m). ISSN 1573269X. doi:10.1007/s11071-020-05817-x.

[7] McNamara, J. J. and Friedmann, P. P. (2011). Aeroelastic and aerothermoelastic analysis in hypersonic flow: Past, present, and future. *AIAA Journal*, 49(6), 1089–1122. ISSN 00011452. doi:10.2514/1.J050882.

[8] Stanford, B. and Beran, P. (2013). Aerothermoelastic topology optimization with flutter and buckling metrics. *Structural and Multidisciplinary Optimization*, 48(1), 149–171. ISSN 1615147X. doi:10.1007/s00158-013-0885-x.

[9] Deaton, J. D. and Grandhi, R. V. (2015). Significance of geometric nonlinearity in the design of thermally loaded structures. *Journal of Aircraft*, 52(4), 1226–1234. ISSN 15333868. doi:10.2514/1.C032872.

[10] Lee, J. and Bhatia, M. (2019). Impact of corrugations on bifurcation and thermoelastic responses of hat-stiffened panels. *Thin-Walled Structures*, 140(October 2018), 209–221. ISSN 02638231. doi:10.1016/j.tws.2019.03.027.

[11] Bhatia, M. and Beran, P. (2017). Design of thermally stressed panels subject to transonic flutter constraints. *Journal of Aircraft*, 54(6), 2340–2349. ISSN 15333868. doi:10.2514/1.C034301.

[12] McHugh, K. A. and Deaton, J. D. (2022). Modal Design Optimization for Panel Flutter and Buckling. *Proceedings of the International Forum of Aeroelasticity and Structural Dynamics 2022, IFASD 2022*, (June).

[13] Freydin, M., Dowell, E. H., Whalen, T. J., et al. (2020). A theoretical computational model of a plate in hypersonic flow. *Journal of Fluids and Structures*, 93, 102858. ISSN 10958622. doi:10.1016/j.jfluidstructs.2019.102858.

[14] Leszcz, C. (2023). Multi-Fidelity Design of Flexible Aircraft Structures in High-Speed, High-Temperature Flow.

[15] Riley, Z. B., Perez, R., and Brouwer, K. R. (2023). Design of Aerothermoelastic Experiments in the AFRL Mach 6 High Reynolds Number Facility. (January), 1–16. doi:10.2514/6.2023-0948.

[16] (1994). *Metallic Materials and Elements for Aerospace Vehicle Structures*. Department of Defense.

[17] Anderson, J. (2017). *Fundamentals of Aerodynamics*. New York: McGraw Hill, sixth ed. ISBN 9781259129919.

[18] Freydin, M., Dowell, E. H., Currao, G. M., et al. (2019). Computational study for the design of a hypersonic panel flutter experiment. *International Forum on Aeroelasticity and Structural Dynamics 2019, IFASD 2019*, (June), 1–17.

[19] Freydin, M. and Dowell, E. H. (2021). Nonlinear Theoretical Aeroelastic Model of a Plate : Free to Fixed In-Plane Boundaries. *AIAA Journal*, 59(2), 447–461. doi:10.2514/1.J059551.

[20] Haftka, R. T., Gürdal, Z., and Kamat, M. P. (1992). *Elements of Structural Optimization. Third revised and expanded edition*, vol. 1. ISBN 978-94-015-7864-6.

[21] Eckert, E. R. G. (1956). Engineering Relations for Heat Transfer and Friction in High-Velocity Laminar and Turbulent Boundary-Layer Flow Over Surfaces With Constant Pressure and Temperature. *Journal of Fluids Engineering*, 78(6), 1273–1283. ISSN 0097-6822. doi:10.1115/1.4014011.

[22] Dowell, E. H. (2022). *A Modern Course in Aeroelasticity*. Springer International Publishing, sixth ed. ISBN 9783030742355.

A PLATE DERIVATION

We begin with the potential energy of a plate.

$$U = \frac{1}{2} \int\limits_{-\frac{h}{2}}^{\frac{h}{2}} \int\limits_{0}^{L_y} \int\limits_{0}^{L_x} \left(\sigma_x \epsilon_x + \sigma_y \epsilon_y + \sigma_{xy} \epsilon_{xy} \right) \; dx \; dy \; dz \tag{15}$$

$$\epsilon_x = u_x + \frac{1}{2} w_x^2 - z w_{xx} \tag{16}$$

$$\epsilon_y = v_y + \frac{1}{2} w_y^2 - z w_{yy} \tag{17}$$

$$\epsilon_{xy} = u_y + v_x + w_x w_y - 2 z w_{xy} \tag{18}$$

$$\sigma_x = \frac{E}{1 - \nu^2} \left(\epsilon_x + \nu \epsilon_y - \alpha(1 + \nu)\Delta T \right) \tag{19}$$

$$\sigma_y = \frac{E}{1 - \nu^2} \left(\epsilon_y + \nu \epsilon_x - \alpha(1 + \nu)\Delta T \right) \tag{20}$$

$$\sigma_{xy} = \frac{E}{2 \left(1 + \nu \right)} \epsilon_{xy} \tag{21}$$

$$\begin{aligned}
U = \iint \frac{D(x,y)}{2} & \left(w_{xx}^2 + w_{yy}^2 + 2\nu w_{yy} w_{xx} + 2 \left(1 - \nu \right) w_{xy}^2 \right) \\
& + \frac{h(x,y)E}{2 \left(1 - \nu^2 \right)} \Bigg(u_x^2 + v_y^2 + w_y^2 v_y + u_x w_x^2 + 1/4 w_y^4 + 1/4 w_x^4 + 1/2 w_x^2 w_y^2 \\
& \qquad\qquad + \nu \left(2 u_x v_y + w_x^2 v_y + u_x w_y^2 \right) \\
& \qquad - \left(1 + \nu \right) \alpha \Delta T \left(u_x + v_y + 1/2 w_x^2 + 1/2 w_y^2 \right) \\
& \quad + \left(1 - \nu \right) \left(u_y v_x + w_x w_y u_y + w_x w_y v_x + 1/2 u_y^2 + 1/2 v_x^2 \right) \Bigg) \; dx \; dy
\end{aligned} \tag{22}$$

Using the Galerkin method, we can discretize and perform separation of variables on the equation of motion in the typical manner by expanding w in Eqn. 1 as follows.

$$w(x, y, t) = \sum_j \psi_j(x,y) q_j(t) = \mathbf{\Psi_w q} \tag{23}$$

Although more generally ψ_j can be any function which satisfies the geometric boundary conditions, here ψ_j is the natural mode shape for a clamped-clamped beam multiplied by itself to cover two dimensional space.

$$U = \iint \frac{D(x,y)}{2} \left(\psi_{xx_i}^w \psi_{xx_j}^w + \psi_{yy_i}^w \psi_{yy_j}^w + 2\nu \psi_{xx_i}^w \psi_{yy_j}^w + 2\left(1-\nu\right) \psi_{xy_i}^w \psi_{xy_j}^w \right) w_i w_j$$

$$+ \frac{h(x,y)E}{2\left(1-\nu^2\right)} \left(\psi_{x_i}^u \psi_{x_j}^u u_i u_j + \psi_{y_i}^v \psi_{y_j}^v v_i v_j + \psi_{y_i}^w \psi_{y_j}^w \psi_{y_k}^v w_i w_j v_k + \psi_{x_i}^w \psi_{x_j}^w \psi_{x_k}^u w_i w_j u_k \right.$$

$$+ \frac{1}{4} \left(\psi_{y_i}^w \psi_{y_j}^w \psi_{y_k}^w \psi_{y_l}^w + \psi_{x_i}^w \psi_{x_j}^w \psi_{x_k}^w \psi_{x_l}^w + 2\psi_{x_i}^w \psi_{x_j}^w \psi_{y_k}^w \psi_{y_l}^w \right) w_i w_j w_k w_l$$

$$+ \nu \left(2\psi_{x_i}^u \psi_{y_j}^v u_i v_j + \psi_{x_i}^w \psi_{x_j}^w \psi_{y_k}^v w_i w_j v_k + \psi_{y_i}^w \psi_{y_j}^w \psi_{x_k}^u w_i w_j u_k \right)$$

$$- \left(1+\nu\right) \alpha \Delta T \left(\psi_{x_i}^u u_i + \psi_{y_i}^v v_i + 1/2\psi_{x_i}^w \psi_{x_j}^w w_i w_j + 1/2\psi_{y_i}^w \psi_{y_j}^w w_i w_j \right)$$

$$+ \left(1-\nu\right) \left(\psi_{y_i}^u \psi_{x_j}^v u_i v_j + \psi_{x_i}^w \psi_{y_j}^w \psi_{y_k}^u w_i w_j u_k + \psi_{x_i}^w \psi_{y_j}^w \psi_{x_k}^v w_i w_j v_k \right.$$

$$\left. \left. + 1/2\psi_{y_i}^u \psi_{y_j}^u u_i u_j + 1/2\psi_{x_i}^v \psi_{x_j}^v v_i v_j \right) dx\,dy \quad (24)$$

$$\frac{\partial U}{\partial w} = \frac{\partial U}{\partial w_i} + \frac{\partial U}{\partial w_j} + \frac{\partial U}{\partial w_k} + \frac{\partial U}{\partial w_l} \quad (25)$$

Taking the derivative with respect to each displacement coordinate starting with w and simplifying:

$$\frac{\partial U}{\partial w} = \iint D(x,y) \left(\psi_{xx_i}^w \psi_{xx_j}^w + \psi_{yy_i}^w \psi_{yy_j}^w + \nu \left(\psi_{xx_i}^w \psi_{yy_j}^w + \psi_{yy_i}^w \psi_{xx_j}^w \right) + 2\left(1-\nu\right) \psi_{xy_i}^w \psi_{xy_j}^w \right) w_j$$

$$+ \frac{h(x,y)E}{2\left(1-\nu^2\right)} \left(\left(2\psi_{x_i}^w \psi_{x_j}^w \psi_{x_k}^u + 2\nu\psi_{y_i}^w \psi_{y_j}^w \psi_{x_k}^u + \left(1-\nu\right) \left(\psi_{x_i}^w \psi_{y_j}^w \psi_{y_k}^u + \psi_{y_i}^w \psi_{x_j}^w \psi_{y_k}^u \right) \right) w_j u_k \right.$$

$$+ \left(2\psi_{y_i}^w \psi_{y_j}^w \psi_{y_k}^v + 2\nu\psi_{x_i}^w \psi_{x_j}^w \psi_{y_k}^v + \left(1-\nu\right) \left(\psi_{x_i}^w \psi_{y_j}^w \psi_{x_k}^v + \psi_{y_i}^w \psi_{x_j}^w \psi_{x_k}^v \right) \right) w_j v_k$$

$$+ \left(\psi_{y_i}^w \psi_{y_j}^w \psi_{y_k}^w \psi_{y_l}^w + \psi_{x_i}^w \psi_{x_j}^w \psi_{x_k}^w \psi_{x_l}^w + \psi_{x_i}^w \psi_{x_j}^w \psi_{y_k}^w \psi_{y_l}^w + \psi_{y_i}^w \psi_{y_j}^w \psi_{x_k}^w \psi_{x_l}^w \right) w_j w_k w_l$$

$$\left. - \left(1+\nu\right) \alpha \Delta T \left(\psi_{x_i}^w \psi_{x_j}^w + \psi_{y_i}^w \psi_{y_j}^w \right) w_j \right) dx\,dy \quad (26)$$

$$\frac{\partial U}{\partial w} = K_{ij} w_j + N_{ijk}^{(b)} w_j u_k + N_{ijk}^{(c)} w_j v_k + N_{ijkl}^{(a)} w_j w_k w_l - K_{ij}^{TH} w_j \quad (27)$$

$$K_{ij} = \frac{E}{12\left(1-\nu^2\right)} \iint h(x,y)^3 \left(\psi_{xx_i}^w \psi_{xx_j}^w + \psi_{yy_i}^w \psi_{yy_j}^w \right.$$

$$\left. + \nu \left(\psi_{xx_i}^w \psi_{yy_j}^w + \psi_{yy_i}^w \psi_{xx_j}^w \right) + 2\left(1-\nu\right) \psi_{xy_i}^w \psi_{xy_j}^w \right) dx\,dy \quad (28)$$

26

$$N_{ijk}^{(b)} = \frac{E}{2\left(1-\nu^2\right)} \iint h(x,y) \left(2\psi_{x_i}^w \psi_{x_j}^w \psi_{x_k}^u + 2\nu \psi_{y_i}^w \psi_{y_j}^w \psi_{x_k}^u + (1-\nu)\left(\psi_{x_i}^w \psi_{y_j}^w \psi_{y_k}^u + \psi_{y_i}^w \psi_{x_j}^w \psi_{y_k}^u \right) \right) dx\,dy$$

(29)

$$N_{ijk}^{(c)} = \frac{E}{2\left(1-\nu^2\right)} \iint h(x,y) \left(2\psi_{y_i}^w \psi_{y_j}^w \psi_{y_k}^v + 2\nu \psi_{x_i}^w \psi_{x_j}^w \psi_{y_k}^v + (1-\nu)\left(\psi_{x_i}^w \psi_{y_j}^w \psi_{x_k}^v + \psi_{y_i}^w \psi_{x_j}^w \psi_{x_k}^v \right) \right) dx\,dy$$

(30)

$$N_{ijkl}^{(a)} = \frac{E}{2\left(1-\nu^2\right)} \iint h(x,y) \left(\psi_{y_i}^w \psi_{y_j}^w \psi_{y_k}^w \psi_{y_l}^w + \psi_{x_i}^w \psi_{x_j}^w \psi_{x_k}^w \psi_{x_l}^w + \psi_{x_i}^w \psi_{x_j}^w \psi_{y_k}^w \psi_{y_l}^w + \psi_{y_i}^w \psi_{y_j}^w \psi_{x_k}^w \psi_{x_l}^w \right) dx\,dy$$

(31)

$$K_{ij}^{TH} = \frac{E\alpha\left(1+\nu\right)}{2\left(1-\nu^2\right)} \iint \Delta T h(x,y) \left(\psi_{x_i}^w \psi_{x_j}^w + \psi_{y_i}^w \psi_{y_j}^w \right) dx\,dy$$

(32)

Similarly for the derivative in u:

$$\frac{\partial U}{\partial u} = \iint \frac{h(x,y)E}{2\left(1-\nu^2\right)} \Bigg(\left(2\psi_{x_i}^u \psi_{x_j}^u + (1-\nu)\psi_{y_i}^u \psi_{y_j}^u \right) u_j + \left(2\nu \psi_{x_i}^u \psi_{y_j}^v + (1-\nu)\psi_{y_i}^u \psi_{x_j}^v \right) v_j$$

$$+ \left(\psi_{x_j}^w \psi_{x_k}^w \psi_{x_i}^u + \nu \psi_{y_j}^w \psi_{y_k}^w \psi_{x_i}^u + (1-\nu)\psi_{y_i}^u \psi_{y_j}^w \psi_{x_k}^w \right) w_j w_k - (1+\nu)\,\alpha \Delta T \psi_{x_i}^u \Bigg) dx\,dy \quad (33)$$

$$\frac{\partial U}{\partial u} = G_{ij}^u u_j + H_{ij} v_j + I_{ijk}^u w_j w_k - K_i^{TH_u}$$

(34)

$$G_{ij}^u = \frac{E}{2\left(1-\nu^2\right)} \iint h(x,y) \left(2\psi_{x_i}^u \psi_{x_j}^u + (1-\nu)\psi_{y_i}^u \psi_{y_j}^u \right) dx\,dy$$

(35)

$$H_{ij} = \frac{E}{2\left(1-\nu^2\right)} \iint h(x,y) \left(2\nu \psi_{x_i}^u \psi_{y_j}^v + (1-\nu)\psi_{y_i}^u \psi_{x_j}^v \right) dx\,dy$$

(36)

$$I_{ijk}^u = \frac{E}{2\left(1-\nu^2\right)} \iint h(x,y) \left(\psi_{x_j}^w \psi_{x_k}^w \psi_{x_i}^u + \nu \psi_{y_j}^w \psi_{y_k}^w \psi_{x_i}^u + (1-\nu)\psi_{y_i}^u \psi_{y_j}^w \psi_{x_k}^w \right) dx\,dy$$

(37)

$$K_i^{TH_u} = \frac{E\left(1+\nu\right)\alpha}{2\left(1-\nu^2\right)} \iint h(x,y) \Delta T \psi_{x_i}^u \, dx\,dy$$

(38)

And again for the derivative in v:

$$\frac{\partial U}{\partial v} = \iint \frac{h(x,y)E}{2\left(1-\nu^2\right)} \Bigg(\left(2\nu \psi_{y_i}^v \psi_{x_j}^u + (1-\nu)\psi_{x_i}^v \psi_{y_j}^u \right) u_j + \left(2\psi_{y_i}^v \psi_{y_j}^v + (1-\nu)\psi_{x_i}^v \psi_{x_j}^v \right) v_j$$

$$+ \left(\psi_{y_j}^w \psi_{y_k}^w \psi_{y_i}^v + \nu \psi_{x_j}^w \psi_{x_k}^w \psi_{y_i}^v + (1-\nu)\psi_{x_i}^v \psi_{x_j}^w \psi_{y_k}^w \right) w_j w_k - (1+\nu)\,\alpha \Delta T \psi_{y_i}^v \Bigg) dx\,dy \quad (39)$$

$$\frac{\partial U}{\partial v} = H_{ji} u_j + G_{ij}^v v_j + I_{ijk}^v w_j w_k - K_i^{TH_v}$$

(40)

$$G_{ij}^v = \frac{E}{2\left(1-\nu^2\right)} \iint h(x,y) \left(2\psi_{y_i}^v \psi_{y_j}^v + (1-\nu)\psi_{x_i}^v \psi_{x_j}^v\right) \, dx \, dy \tag{41}$$

$$I_{ijk}^v = \frac{E}{2\left(1-\nu^2\right)} \iint h(x,y) \left(\psi_{y_j}^w \psi_{y_k}^w \psi_{y_i}^v + \nu\psi_{x_j}^w \psi_{x_k}^w \psi_{y_i}^v + (1-\nu)\psi_{x_i}^v \psi_{x_j}^w \psi_{y_k}^w\right) \, dx \, dy \tag{42}$$

$$K_i^{TH_v} = \frac{E\left(1+\nu\right)\alpha}{2\left(1-\nu^2\right)} \iint h(x,y)\Delta T \psi_{y_i}^v \, dx \, dy \tag{43}$$

$$T = \frac{1}{2} \iint \int \rho\left(w_t^2 + u_t^2 + v_t^2\right) \, dx \, dy \, dz \tag{44}$$

$$T = \frac{1}{2} \iint h(x,y)\rho\left((\psi^w w_t)^2 + (\psi^u u_t)^2 + (\psi^v v_t)^2\right) \, dx \, dy \tag{45}$$

$$\frac{\partial}{\partial t}\frac{\partial T}{\partial w_t} = \iint h(x,y)\rho\psi^w\psi^w w_{tt} \, dx \, dy = M_{ij}w_{tt_j} \tag{46}$$

$$\frac{\partial}{\partial t}\frac{\partial T}{\partial u_t} = \iint h(x,y)\rho\psi^u\psi^u u_{tt} \, dx \, dy = M_{ij}^u u_{tt_j} \tag{47}$$

$$\frac{\partial}{\partial t}\frac{\partial T}{\partial v_t} = \iint h(x,y)\rho\psi^v\psi^v v_{tt} \, dx \, dy = M_{ij}^v v_{tt_j} \tag{48}$$

$$M_{ij}w_{tt_j} + K_{ij}w_j + N_{ijk}^{(b)}w_j u_k + N_{ijk}^{(c)}w_j v_k + N_{ijkl}^{(a)}w_j w_k w_l - K_{ij}^{TH}w_j = Q_i \tag{49}$$

$$M_{ij}^u u_{tt_j} + G_{ij}^u u_j + H_{ij}v_j + I_{ijk}^u w_j w_k - K_i^{TH_u} = 0 \tag{50}$$

$$M_{ij}^v v_{tt_j} + H_{ji}u_j + G_{ij}^v v_j + I_{ijk}^v w_j w_k - K_i^{TH_v} = 0 \tag{51}$$

$$Q_i = -\iint \Delta p \psi_i^w \, dx \, dy \tag{52}$$

$$\Delta p = \frac{\rho_\infty U_\infty}{M_\infty}\left(w_t + U_\infty w_x\right) \tag{53}$$

$$= \frac{\rho_\infty U_\infty}{M_\infty}\left(\psi_j^w w_{t_j} + U_\infty \psi_{x_j}^w w_j\right) \tag{54}$$

$$Q_i = -\frac{\rho_\infty U_\infty}{M_\infty}\iint \psi_i^w \psi_j^w \, dx \, dy \, w_{t_j} - \frac{\rho_\infty U_\infty^2}{M_\infty}\iint \psi_i^w \psi_{x_j}^w \, dx \, dy \, w_j \tag{55}$$

$$Q_i = -C_{ij}^A w_{t_j} - K_{ij}^A \, w_j \tag{56}$$

$$M_{ij}w_{tt_j} + C_{ij}^A w_{t_j} + \left(K_{ij} + K_{ij}^A - K_{ij}^{TH}\right)w_j + N_{ijkl}^{(a)}w_j w_k w_l + N_{ijk}^{(b)}w_j u_k + N_{ijk}^{(c)}w_j v_k = 0 \tag{57}$$

$$M_{ij}^u u_{tt_j} + G_{ij}^u u_j + H_{ij}v_j + I_{ijk}^u w_j w_k - K_i^{TH_u} = 0 \tag{58}$$

$$M_{ij}^v v_{tt_j} + H_{ji}u_j + G_{ij}^v v_j + I_{ijk}^v w_j w_k - K_i^{TH_v} = 0 \tag{59}$$

To solve this system of equations, let's make a simplification that comes from Freydin [19]. Neglecting the in-plane acceleration u_{tt} and v_{tt}, we can solve for the in-plane displacements as an algebraic function of the out-of-plane displacements w.

$$
\begin{bmatrix} G^u_{mk} & H_{mk} \\ H_{km} & G^v_{mk} \end{bmatrix} \begin{Bmatrix} u_k \\ v_k \end{Bmatrix} = \begin{Bmatrix} -I^u_{mno}w_n w_o + K^{TH_u}_m \\ -I^v_{mno}w_n w_o + K^{TH_v}_m \end{Bmatrix} \tag{60}
$$

$$
M_{ij}w_{tt_j} + C^A_{ij}w_{t_j} + \left(K_{ij} + K^A_{ij} - K^{TH}_{ij} \right) w_j + N^{(a)}_{ijkl}w_j w_k w_l + \begin{bmatrix} N^{(b)}_{ijk}w_j & N^{(c)}_{ijk}w_j \end{bmatrix} \begin{Bmatrix} u_k \\ v_k \end{Bmatrix} = 0 \tag{61}
$$

$$
\begin{aligned}
M_{ij}w_{tt_j} + C^A_{ij}w_{t_j} &+ \left(K_{ij} + K^A_{ij} - K^{TH}_{ij} \right) w_j + N^{(a)}_{ijkl}w_j w_k w_l \\
&+ \begin{bmatrix} N^{(b)}_{ijk}w_j & N^{(c)}_{ijk}w_j \end{bmatrix} \begin{bmatrix} G^u_{mk} & H_{mk} \\ H_{km} & G^v_{mk} \end{bmatrix}^{-1} \begin{Bmatrix} -I^u_{mno}w_n w_o + K^{TH_u}_m \\ -I^v_{mno}w_n w_o + K^{TH_v}_m \end{Bmatrix} = 0
\end{aligned} \tag{62}
$$

$$
\begin{aligned}
M_{ij}w_{tt_j} + C^A_{ij}w_{t_j} &+ \left(K_{ij} + K^A_{ij} - K^{TH}_{ij} \right) w_j + N^{(a)}_{ijkl}w_j w_k w_l \\
&+ \begin{bmatrix} N^{(b)}_{ijk}w_j & N^{(c)}_{ijk}w_j \end{bmatrix} \begin{bmatrix} G^u_{mk} & H_{mk} \\ H_{km} & G^v_{mk} \end{bmatrix}^{-1} \left(\begin{Bmatrix} -I^u_{mno}w_n w_o \\ -I^v_{mno}w_n w_o \end{Bmatrix} + \begin{Bmatrix} K^{TH_u}_m \\ K^{TH_v}_m \end{Bmatrix} \right) = 0
\end{aligned} \tag{63}
$$

$$
\begin{aligned}
M_{ij}w_{tt_j} + C^A_{ij}w_{t_j} &+ \left(K_{ij} + K^A_{ij} - K^{TH}_{ij} \right) w_j + N^{(a)}_{ijkl}w_j w_k w_l \\
&+ \begin{bmatrix} N^{(b)}_{ijk}w_j & N^{(c)}_{ijk}w_j \end{bmatrix} \left(\begin{Bmatrix} \overline{I}^u_{kno}w_n w_o \\ \overline{I}^v_{kno}w_n w_o \end{Bmatrix} + \begin{Bmatrix} \overline{K}^{TH_u}_k \\ \overline{K}^{TH_v}_k \end{Bmatrix} \right) = 0
\end{aligned} \tag{64}
$$

$$
\begin{aligned}
M_{ij}w_{tt_j} + C^A_{ij}w_{t_j} &+ \left(K_{ij} + K^A_{ij} - K^{TH}_{ij} \right) w_j + N^{(a)}_{ijkl}w_j w_k w_l + \tilde{N}^{(b)}_{ijno}w_j w_n w_o + \tilde{N}^{(c)}_{ijno}w_j w_n w_o \\
&+ \tilde{K}^{TH_u}_{ij}w_j + \tilde{K}^{TH_v}_{ij}w_j = 0
\end{aligned} \tag{65}
$$

$$
\boxed{
\begin{aligned}
M_{ij}w_{tt_j} + C^A_{ij}w_{t_j} &+ \left(K_{ij} + K^A_{ij} - K^{TH}_{ij} + \tilde{K}^{TH_u}_{ij} + \tilde{K}^{TH_v}_{ij} \right) w_j \\
&+ \left(N^{(a)}_{ijkl} + \tilde{N}^{(b)}_{ijkl} + \tilde{N}^{(c)}_{ijkl} \right) w_j w_k w_l = 0
\end{aligned}
} \tag{66}
$$

$$
\tilde{K}^{TH_u}_{ij} = N^{(b)}_{ijk}\overline{K}^{TH_u}_k \tag{67}
$$

$$
\tilde{K}^{TH_v}_{ij} = N^{(c)}_{ijk}\overline{K}^{TH_v}_k \tag{68}
$$

Where $\overline{K}_k^{TH_u}$ and $\overline{K}_k^{TH_v}$ are defined by

$$\begin{Bmatrix} \overline{K}_k^{TH_u} \\ \overline{K}_k^{TH_v} \end{Bmatrix} = \begin{bmatrix} G_{mk}^u & H_{mk} \\ H_{km} & G_{mk}^v \end{bmatrix}^{-1} \begin{Bmatrix} K_m^{TH_u} \\ K_m^{TH_v} \end{Bmatrix} \tag{69}$$

$$\tilde{N}_{ijno}^{(b)} = N_{ijk}^{(b)} \overline{I}_{kno}^u \tag{70}$$

$$\tilde{N}_{ijno}^{(c)} = N_{ijk}^{(c)} \overline{I}_{kno}^v \tag{71}$$

Where $\overline{I}_{kno}^u$ and $\overline{I}_{kno}^v$ are defined by

$$\begin{Bmatrix} \overline{I}_{kno}^u \\ \overline{I}_{kno}^v \end{Bmatrix} = \begin{bmatrix} G_{mk}^u & H_{mk} \\ H_{km} & G_{mk}^v \end{bmatrix}^{-1} \begin{Bmatrix} -I_{mno}^u \\ -I_{mno}^v \end{Bmatrix} \tag{72}$$

Note: $\tilde{K}_{ij}^{TH_u}$ and $\tilde{K}_{ij}^{TH_v}$ are 3-4 orders smaller than K_{ij}^{TH}.

B ABAQUS BUILT-IN OPTIMIZATION

An optimization task is set up in Abaqus to compare available high-fidelity optimization with the in-house low-fidelity modal code. This is not without its challenges, as Abaqus's structural code is not directly coupled with an aerothermal code. Indeed, in this work the coupling is done manually, see Sec. 4. In addition, the computational cost is much greater than the in-house method.

The optimization task is created with a constant temperature field that represents the maximum temperature found on the panel from the heat transfer analysis, which is 318°F, and non-temperature dependent material properties. This is to create a better comparison to the modal optimization code, which does not implement the temperature field from the heat transfer analysis, but rather uses the maximum value and also implements constant material properties. An initial stress analysis is performed using the same procedure as detailed previously to complete a stress analysis on the 0.075 inch uniform panel with the material properties of Stainless Steel 17-4PH H900 at 200°F. The mesh must be coarsened to reduce the computational cost of the optimization task. The resulting stress distribution is shown in Fig. 21. The maximum stress found on the panel is 241,400 psi, the maximum displacement is 0.1513 inches, and the initial weight is 0.637 pounds. This maximum stress and displacement is much greater than what was found when applying a varying temperature field across the panel and implementing temperature dependent material properties. The maximum stress was 47,900 psi and the maximum displacement was 0.0128 inches.

Four optimization tasks are explored, each with different optimization functions and constraints. Three tasks are set to minimize weight with a constraint on the strain energy to be less than or equal to 80%, 90%, and 100% of the initial value, for each respective case. Another task is to minimize the strain energy with a constraint on the weight to be less than 90% of its initial value. For each case, a geometric constraint is set so that the panel thickness cannot go below 0.01 inches, which is the minimum thickness that can be manufactured. The resulting percent changes in stress, displacement, and weight are shown in Table 4. By requiring the optimizer to minimize weight while keeping the same strain energy, the panel weight is reduced by 21.77%. This weight reduction is greater than the in-house code achieves, however with the large caveats that this analysis cannot consider whether the panel is buckled, and this analysis is orders of magnitude more costly than the in-house solution.
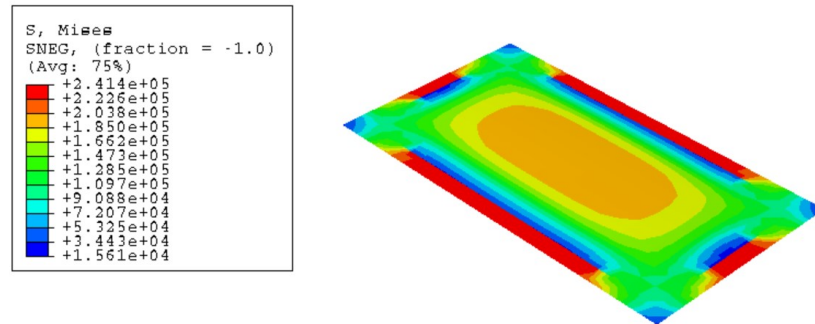
Figure 21: Stress distribution for 0.075 inch panel with constant panel temperature

Table 4: Mass, stress, displacement, and savings for different optimization tasks

Optimization task	Initial	Min weight, SE ≤ 80%	Min weight, SE ≤ 90%	Min weight, SE ≤ 100%	Min SE, weight ≤ 90%
Mass [lb]	0.637	0.765	0.623	0.498	0.573
Mass [kg]	0.289	0.347	0.283	0.226	0.260
Mass Savings [%]	-	-20.01	2.24	21.77	10
Stress [psi]	241400	244900	240500	238400	237900
Stress Savings [%]	-	-1.45	0.37	1.24	1.45
Displacement [in]	0.1513	0.1334	0.1389	0.1505	0.1454
Displacement Savings [%]	-	11.83	8.19	0.53	3.9